

Contents lists available at ScienceDirect

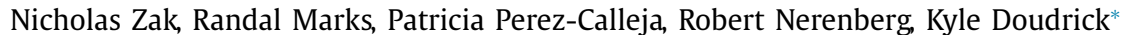
Water Research

journal homepage: www.elsevier.com/locate/watres



eps

A computational model for the catalytic hydrogel membrane reactor



University of Notre Dame, Department of Civil and Environmental Engineering and Earth Sciences, 156 Fitzpatrick Hall, 46556 Notre Dame, IN, USA



ARTICLE INFO

Article history: Received 3 February 2020 Revised 16 July 2020 Accepted 17 July 2020 Available online 185

Keywords: CHMR Catalyst Hydrogenation Hydrogel AQUASIM

ABSTRACT

The catalytic hydrogel membrane reactor (CHMR) is a promising new technology for hydrogenation of aqueous contaminants in drinking water. It offers numerous benefits over conventional three-phase reactors, including immobilization of nano-catalysts, high reactivity, and control over the hydrogen (H2) supply concentration. In this study, a computational model of the CHMR was developed using AQUASIM and calibrated with 32 experimental datasets for a nitrite (NO₂⁻)-reducing CHMR using palladium (Pd) nano-catalysts (~4.6 nm). The model was then used to identify key factors impacting the behavior of the CHMR, including hydrogel catalyst density, H₂ supply pressure, influent and bulk NO₂- concentrations, and hydrogel thickness. Based on the model calibration, the reaction rate constants for the NO₂- steadystate adsorption Hinshelwood reaction equation, k_1 and k_2 , were 0.0039 m³ mole-Pd⁻¹ s⁻¹ and 0.027 (mole-H₂ m³)^{1/2} mole-Pd⁻¹ s⁻¹, respectively. The reactant flux, which is the overall NO_2 removal rate for the CHMR, is affected by the NO2- reduction rate at each catalyst site, which is in turn controlled by the available NO₂⁻ and H₂ concentrations that are regulated by their mass transport behavior. Reactant transport in the CHMR is counter-diffusional. So for thick hydrogels, the concurrent concentrations of NO₂⁻ and H₂ are limiting in the middle region along the x-y plane of the hydrogel, which results in a low overall NO2- removal rate (i.e., flux). Thinner hydrogels provide higher concurrent reactant concentrations throughout the hydrogel, resulting in higher fluxes. However, if the hydrogel is too thin, the flux becomes limited by the amount of Pd that can be loaded, and unused H2 can diffuse into the bulk and promote biofilm growth. The hydrogel thickness that maximized the NO₂- flux ranged between 30 and 150 μm for the conditions tested. The computational model is the first to describe CHMR behavior, and it is an important tool for the further development of the CHMR. It also can be adapted to assess CHMR behavior for other contaminants or catalysts or used for other types of interfacial catalytic membrane reactors.

© 2020 Elsevier Ltd. All rights reserved.

1. Introduction

Heterogeneous hydrogenation catalysis (HHC) is an effective approach for treating water containing oxidized contaminants such as nitrate, nitrite, bromate, chlorate, and perchlorate (Chaplin et al., 2012). In HHC, hydrogen (H₂) dissociates on the catalyst's surface to form highly reactive metal hydrides that can subsequently reduce the adsorbed contaminant. In conventional three-phase HHC reactors (e.g., packed-bed, bubble column), $H_{2(g)}$ is typically bubbled directly into solution or water droplets are dispersed in the gas. This poses numerous complications, including mass-transfer limitations, low $H_{2(g)}$ solubility in water, loss of $H_{2(g)}$ with the off gases, and safety concerns due to the combustibility of $H_{2(g)}$ (Bergquist, 2017; Bertoch et al., 2017; Choe et al., 2015).

An emerging type of HHC reactor that offers numerous benefits over conventional three-phase reactors is the interfacial catalytic membrane reactor (ICMR) (Aran et al., 2011; Buonomenna et al., 2010; Chen et al., 2003; Daub et al., 1999; Dittmeyer et al., 2001; Dittmeyer et al., 2004; Espinosa et al., 2016; Espinosa et al., 2018; Postma et al., 2018; Strukul et al., 2000). An ICMR typically consists of a permeable membrane that separates the gas and liquid phases and the solid catalyst is in contact with the membrane. For a gas-permeable membrane used for HHC, $H_{2(g)}$ diffuses through the membrane wall and enters the liquid phase in a dissolved state. Because H2 is dissolved in solution, the gas-liquid diffusive barrier at the catalyst surface is eliminated and provides better overall transport kinetics. The catalyst in an ICMR is typically loaded directly onto the membrane surface or bound within an inorganic/organic shell that is on the membrane. It provides improved catalytic activity, control over $H_{2(g)}$ supply concentrations, greater H₂ transfer and use efficiency, and catalyst immobilization.

The catalytic hydrogel membrane reactor (CHMR) was developed as a new ICMR for water treatment (Marks et al., 2020;

^{*} Corresponding author. E-mail address: kdoudrick@nd.edu (K. Doudrick).

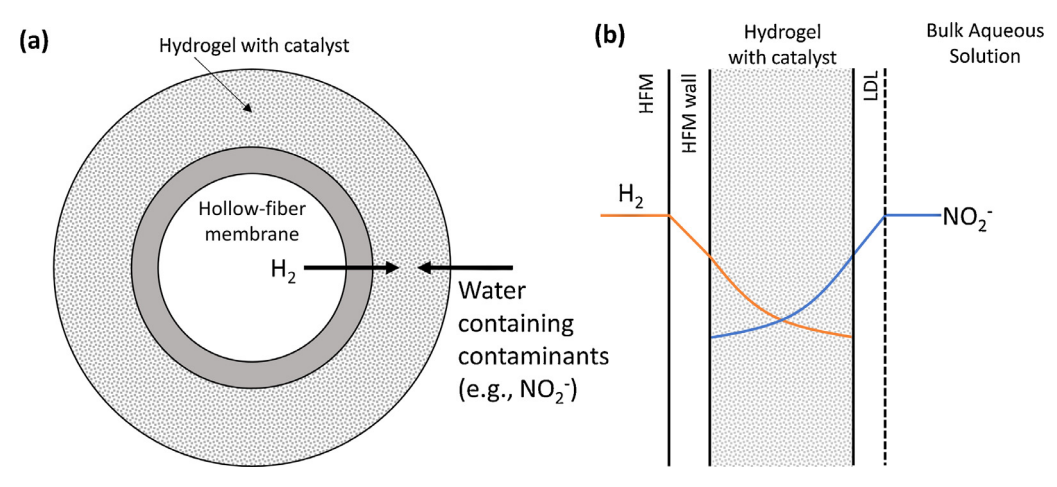


Fig. 1. Schematic of (a) cross-section of the CHMR and (b) contaminant profile of CHMR, NO_2^- is shown as a model contaminant.

Marks et al., 2019). The CHMR consists of a gas-permeable hollowfiber membrane (HFM) pressurized with $H_{2(g)}$ to deliver H_2 directly to a catalyst-bearing hydrogel layer coated on the HFM outer surface (Fig. 1a). This provides numerous advantages over previous ICMRs. For example, it is possible to regulate the H2 transfer fluxes and concentrations within the hydrogel by regulating the H₂ gas pressure in the HFM; there is no bulk-liquid diffusive boundary resistance for H₂ delivery to the hydrogel (Nerenberg, 2016); the gas-transfer efficiency can be as high as 100% if closed-end HFMs are used (Brindle et al., 1998; Hibiya et al., 2003; Martin and Nerenberg, 2012; Pankhania et al., 1999; Perez-Calleja et al., 2017; Syron and Casey, 2008); higher removal rates per mass of catalyst are obtained because the catalyst is uniformly dispersed within a hydrogel rather than layered onto a surface; and by using bundles of small-diameter HFMs, typically with outer diameters of 300 -600 μ m, high volumetric treatment rates can be achieved. Currently, the CHMR faces technical unknowns and barriers, including the long-term mechanical stability of the hydrogel, catalyst deactivation, and a lack of uniform hydrogel thickness along the HFM (Marks et al., 2020; Marks et al., 2019). Developing a predictive model will be useful for understanding the controls on these issues that will allow the CHMR to be optimized.

The CHMR operates by counter-diffusional transport, where H₂ and the target contaminant (e.g., NO₂⁻) diffuse into the catalytic hydrogel from the HFM wall and bulk aqueous solution, respectively (Fig. 1b). These contaminant fluxes are primarily determined by their concentrations within the hydrogel and the intrinsic catalytic reaction rates; these are coupled because the concentrations in the hydrogel are affected by the reaction rates, which in turn affects concentrations. The concentrations in the hydrogel are also affected by the membrane and bulk concentrations of the H₂ and contaminant, respectively, the membrane diffusional resistance, the boundary layer resistance at the hydrogel-water interface, and the hydrogel thickness (Marks et al., 2020; Marks et al., 2019). Given the numerous affecting variables and coupled behavior, a model is needed to better understand the rate-limiting factors and to optimize the reactor performance. Similar models exist to describe counter-diffusional biofilm performance (Essila et al., 2000; Semmens and Essila, 2001), yet no such model exists for the CHMR.

The objective of this study was to develop a one-dimensional (1-D) computational model of the CHMR. The model was calibrated with experimental data (Marks et al., 2020) and then used to describe the variables that control the performance of the CHMR. Specifically, the model was used to evaluate the effect of the hydrogel catalyst density, $\rm H_2$ supply pressure, influent and bulk $\rm NO_2^{-1}$

concentration, and hydrogel thickness on the $\rm H_2$ and $\rm NO_2^-$ concentration profiles, the $\rm NO_2^-$ reaction rate profiles, and the $\rm NO_2^-$ flux. Although nitrate ($\rm NO_3^-$) is arguably a more important water contaminant, $\rm NO_2^-$ is an acceptable model contaminant for creating this model because it is the first reduction step for the $\rm NO_3^-$ hydrogenation reaction. $\rm NO_3^-$ would be a logical extension of the model using data from a suitable catalyst (e.g., a Pd-In catalyst (Guo et al., 2018)). This is the first available computation model that describes the novel CHMR. It can be extended to any catalyst or reactant, allowing for the input of different reaction expressions and reactor conditions, and it can be applied to describe the behavior of other types of ICMRs.

2. Model description

2.1. Model setup

A 1-D model of the CHMR was constructed using the AQUASIM program (Version 2.1), an environmental simulation software for aquatic systems (Reichert, 1994). AQUASIM allows for compartments (e.g., completely-mixed reactor) to be coupled through either advective or diffusive links and analyzed as a single system. The software includes a "biofilm reactor compartment," which is terminology taken directly from AQUASIM and is an analogue for the catalytic hydrogel in the CHMR (Wanner and Morgenroth, 2004). The catalytic hydrogel can be modeled as a "biofilm" without growth or decay. The catalyst may be considered analogous to autotrophic bacteria that use H₂ as an electron donor for oxyanion reduction (Chung et al., 2006; Nerenberg and Rittmann, 2004; Nerenberg et al., 2002; Ziv-El and Rittmann, 2009).

The CHMR model consists of five distinct regions, including (1) the H_2 -supplying HFM lumen, (2) the HFM wall, (3) the catalytic hydrogel, (4) the liquid diffusion layer (LDL), and (5) the well-mixed bulk aqueous solution (Fig. 2). These regions operate under defined conditions and parameters. The HFM lumen is modeled as a mixed reactor compartment containing only $H_{2(g)}$ at a specified partial pressure. The catalytic hydrogel, LDL, and bulk solution are modeled as a biofilm reactor compartment. The LDL was incorporated into the biofilm compartment as a boundary layer resistance for NO_2^- between the hydrogel and bulk solution. The HFM wall is modeled as a diffusive link between the H_2 -supplying mixed compartment and biofilm reactor compartment. The diffusive link is governed by Henry's Law, H_2 diffusivity for the HFM material, and the HFM wall thickness.

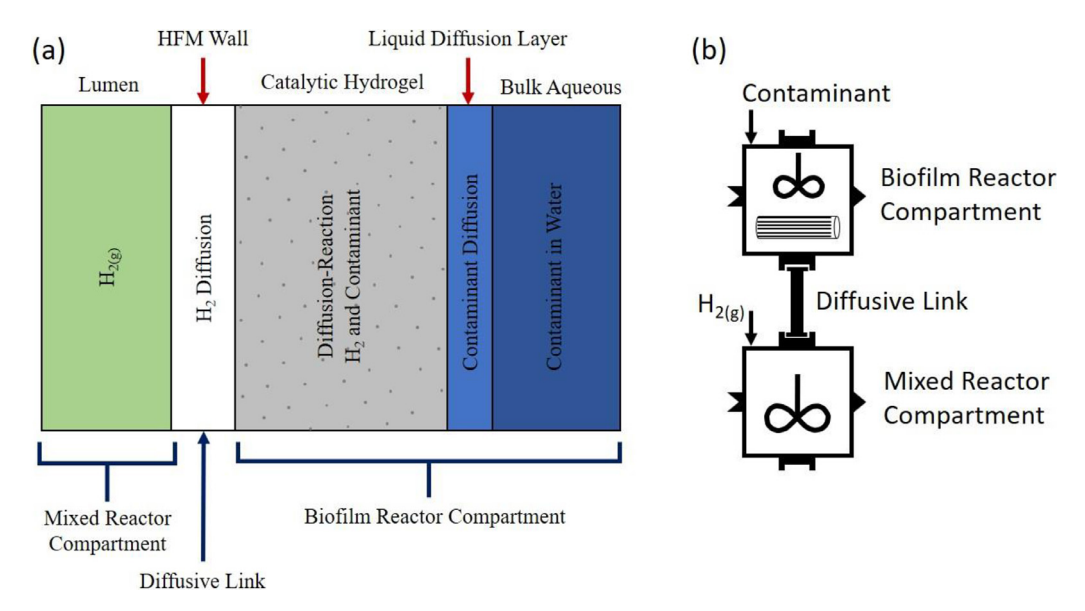


Fig. 2. Schematic depicting the (a) regions of the CHMR and (b) compartments and links in the AQUASIM model. The term "Biofilm Reactor Compartment" is taken directly from AQUASIM, and it is analogous to a catalytic hydrogel reactor compartment.

2.2. Processes

A useful model requires description of the physical and chemical processes that affect reactor performance and reactive species concentrations within the reactor. The primary physical process that influences the reactivity is diffusion, which drives the transport of reactive species within the HFM wall, hydrogel, and LDL. Diffusion is described by Fick's first law (Martin and Nerenberg, 2012), which states that a species will travel from regions of high to low concentrations according to Eq. (1):

$$J = D_e \frac{dC}{dx} \tag{1}$$

where, J is flux (mol m $^{-2}$ s $^{-1}$), D_e is effective diffusivity (m 2 s $^{-1}$), and $\frac{dC}{dx}$ is the concentration gradient of the diffusing species (dC) through the diffusion layer (dx). Flux represents the amount of the species transported through a specific cross-sectional area in a specific amount of time. Fickian diffusion results in a linear concentration gradient across the diffusive regions, including the HFM wall, the non-reactive areas of the hydrogel, and the LDL. The conversion of H_2 from the gas phase to the aqueous phase, as it diffuses through the HFM wall, is governed by the liquid-gas equilibrium constant described by Henry's Law (Martin et al., 2015).

A single chemical reaction process was used in the model, the catalytic hydrogenation of the contaminant. NO_2^- was the contaminant and palladium (Pd) the catalyst. The assumed hydrogenation reaction stoichiometry is described in Equation 2, where 3 moles of H_2 are consumed per 2 moles of NO_2^- .

$$2NO_2^- + 3H_2 + 2H^+ \rightarrow N_2 + 4H_2O$$
 (2)

The reduction rate for the catalytic hydrogenation of NO_2^- using Pd can be described by the steady-state adsorption Hinshelwood model (Hinshelwood, 1940; Shelstad et al., 1960), as validated by Pintar et al. (1998) (Eq. (3)).

$$-r_{NO_{2}^{-}} = C_{cat} \frac{\left(k_{1}C_{NO_{2}^{-}}\right)\left(k_{2}C_{H_{2}}^{-1/2}\right)}{\left(k_{1}C_{NO_{2}^{-}}\right) + \left(k_{2}C_{H_{2}}^{-1/2}\right)}$$
(3)

where, $-r_{NO2-}$ is the NO_2- reduction rate (mole- $NO_2 m^{-3}_{hydrogel}$ s^{-1}), C_{cat} is the molar density of catalyst in the hydrogel (mole-Pd $m^{-3}_{hydrogel}$), k_1 is NO_2- rate constant (m^3 mole- Pd^{-1} s^{-1}), k_2 is H_2 rate constant [(mole- H_2 m^3)^{1/2} mol- Pd^{-1} s^{-1}], C_{NO2-} is the concentration of NO_2- (mole- $NO_2 m^{-3}$),

and C_{H2} is the concentration of H_2 (mole- H_2 m $^{-3}$). Based on the stoichiometry in Eq. (2), the H_2 oxidation rate, r_{H2} , was 1.5 r_{NO2} -(mole- H_2 m $^{-3}$ _{hydrogel} s $^{-1}$).

2.3. Model inputs and calibration

The model provides concentration profiles of NO₂⁻ and H₂ within the catalytic hydrogel and concentrations in the bulk aqueous solution, based on the processes described previously. A complete account of the model parameters is given in Table 1. Reactor configuration parameters, such as flowrate, reactor volume, and HFM (silicone) wall thickness were obtained from previous experimental studies (Marks et al., 2020). The diffusion coefficients for H₂ and NO₂⁻ in water and H₂ in the silicone HFM wall were obtained from previous studies (Ferrell and Himmelblau, 1967; Merkel et al., 2000; Sabba et al., 2017). The diffusivity ratio, f, was estimated from assuming similar diffusion behavior in biofilms (Stewart, 2003) and then adjusted during calibration. The surface area of the hydrogel was calculated assuming it had a perfect cylindrical shape.

The model was calibrated using data from 32 experiments from a previous study on a lab-scale CHMR operated as a completely mixed reactor (Marks et al., 2020). In that study, the NO_2^- reduction rate was evaluated as a function of influent NO_2^- , H_2 supply pressure, and Pd density in the hydrogel. The results of these experiments are provided in Table SI-1. The average hydrogel thickness of fibers used that study were approximately 450 μ m (e.g., Fig. SI-1). But, due to the extreme variability in the hydrogel thickness homogeneity (e.g., gaps), the thickness was considered a variable for fitting in this study and termed the effective hydrogel thickness.

To calibrate the model, the unknown parameters, including the k_1 and k_2 rate constants for the $\mathrm{NO_2}^-$ reduction rate expression (Eq. (3)), the effective hydrogel thickness (l), the diffusivity ratio (f), and the diffusivities of $\mathrm{NO_2}^-$ and $\mathrm{H_2}$ were determined using the AQUASIM parameter estimation tool, which fit time based $\mathrm{NO_2}^-$ concentration profiles to experimental data.

 NO_2^- concentrations for each experimental run were input in the model as real list variables with time as the argument. To allow the model to fit the experimental data, the run conditions (i.e. H_2 pressure, influent NO_2^- concentration, and Pd density) were

Table 1 Model parameters.

Parameter	Value	Units	Source
Influent flowrate, Q _{in}	5.0×10^{-8}	$m^3 s^{-1}$	Marks et al. (2020)
Reactor volume, V	1.2×10^{-4}	m ³	Marks et al. (2020)
Influent NO ₂ -, C _{inf}	0.32 to 5	mole-N m ⁻³	-
H ₂ lumen pressure, pH ₂	0.3 to 4	atm	-
Hydrogel surface area, A	Various	m ² _{hydrogel}	-
Membrane thickness, t	1.524×10^{-4}	m	Marks et al. (2020)
Pd density in the hydrogel, Ccat	10 to 200	mole-Pd m ⁻³ _{hydrogel}	-
^a Hydrogel thickness, <i>l</i>	10 to 800	μ m	-
LDL thickness, LDL	1.0×10^{-4}	m	Marks et al. (2020)
NO_2^- reaction rate constant, k_1	0.0039	m ³ mole-Pd ⁻¹ s ⁻¹	This study
H_2 adsorption constant, k_2	0.027	$(\text{mole-H}_2 \text{ m}^3)^{1/2} \text{ mole-Pd}^{-1} \text{ s}^{-1}$	This study
$^{a}H_{2}$ water diffusion coefficient, D_{H2}	5.5×10^{-9}	$m^2 s^{-1}$	Ferrell and Himmelblau, 1967
H ₂ HFM diffusion coefficient, D _{mem}	1.0×10^{-4}	$m^2 s^{-1}$	Sabba et al. (2017)
^a NO ₂ - water diffusion coefficient, D _{NO2} -	3.8×10^{-9}	$m^2 s^{-1}$	Merkel et al. (2000)
^a Aqueous/hydrogel diffusivity ratio, f	0.97	-	Stewart (2003)
H ₂ Henry's constant, H _{pm}	1280	atm M^{-1}	Benjamin (2015)

^a These values were adjusted during the model calibration.

included as real list variables with calculation number as the argument. In the parameter estimation function, the unknown parameters were set active while the active calculations matched the experimental NO_2^- concentrations to their respective calculation number variables.

The function requires minimum and maximum values for each unknown variable to be considered during numerous iterations minimizing χ^2 . Both rate constants were bound between zero and one, the effective hydrogel thickness was bound between zero and the average hydrogel thickness, the diffusivity ratio was bound between zero and one, and both diffusivities were bound in a range of one half to two times literature values. While the parameter estimation minimized the total χ^2 , the resulting model fit one catalyst loading better than the other. Following the parameter estimation, the rate constants and effective hydrogel thickness were manually adjusted by a trial-and-error approach by minimizing the residual sum of squares (RSS) (Eq. (4)).

$$RSS = \sum_{i=1}^{N} \left(obs_i - cal_i\right)^2 \tag{4}$$

where, cal and obs are the calculated and observed values. The model goodness of fit was determined by the coefficient of determination (R^2) (Eq. (5)).

$$R^{2} = \frac{RSS}{\sum_{i=1}^{N} \left(obs_{i} - \overline{obs}\right)^{2}}$$
 (5)

where, the accent bar represents the mean value. This was calculated by comparing the calculated flux to the observed flux (i.e., Table SI-1)

2.4. Model simulations

The model simulated steady-state behavior for a continuous-flow CHMR. The model was used to evaluate the effect of the hydrogel catalyst density, H_2 supply pressure, influent NO_2^- (and bulk) concentration, and hydrogel thickness on the NO_2^- flux, NO_2^- reaction rate (Eq. (3)), and H_2 and NO_2^- concentration profiles. The NO_2^- flux, J_{NO2^-} (g-N m⁻² d⁻¹), was calculated using Eq. (6).

$$J_{NO_{2}^{-}} = \frac{(Q_{in})(C_{inf} - C_{eff})}{(A)}$$
 (6)

where, C_{inf} is the influent NO₂⁻ concentration (mM) and C_{eff} (mM) is the steady-state bulk concentration. The flux represents the mass of NO₂⁻ removed per day per area of hydrogel. It is equal to the integral of the NO₂⁻ reaction rate profile within the hydrogel, i.e., integration with respect to position within the hydrogel.

3. Results and discussion

3.1. Model calibration

Through the model calibration, NO₂⁻ diffusivity, H₂ diffusivity, and the diffusivity ratio were estimated to be 3.8×10^{-9} m² s⁻¹, 5.5×10^{-9} m² s⁻¹, and 0.97 respectively. Using the AQUASIM parameter estimation, the k_1 , k_2 , and effective hydrogel thickness variables were initially estimated to be $0.0032 \text{ m}^3 \text{ mole-Pd}^{-1} \text{ s}^{-1}$, 0.012 (mole-H₂ m³)^{1/2} mole-Pd⁻¹ s⁻¹, and 106 μ m, respectively. To further improve the fit, these parameters were then manually adjusted to 0.0039 m³ mole-Pd⁻¹ s⁻¹, 0.027 (mole-H₂ m³) $^{1/2}$ mole-Pd⁻¹ s⁻¹, and 100 μ m, respectively. The model was used to calculate theoretical fluxes that were compared to the experimentally calculated fluxes for the conditions tested (Fig. 3; Table SI-1). Overall, the model prediction was very good, with a minimal RSS = 9.9 (Eq. (4)) and an $R^2 = 0.96$ (Eq. (5)), but there were some points that did not lie on their respective model curves. There are a few potential reasons for this deviation. First, for simplicity, the model assumes that N₂ is the sole byproduct with no NH₄⁺ formation; however, the selectivity to N2 and NH4+ shifts with changing H₂ and NO₂⁻ concentrations within the hydrogel (Marks et al., 2020; Marks et al., 2019). This change in the stoichiometry would alter the reduction rates and thus flux. Second, the data is based on single experimental runs and thus there is no statistical error reported. There is presumably some experimental variability, especially at the lower H₂ partial pressure and influent NO₂⁻ experiments where the rates and conversion were low (i.e., bottom curve in Fig. 3b).

As predicted by the model, increasing the Pd density resulted in higher fluxes. Generally, increasing the available $\rm H_2$ or $\rm NO_2^-$ increases the flux. But, at lower $\rm H_2$ supply pressures (<0.3 atm), the reaction became $\rm H_2$ limited, such that increasing the available $\rm NO_2^-$ did not increase the flux. This was more severe for the lower Pd density. The flux is related to the sum of the catalytic rates at each point in the hydrogel. This is controlled by the available $\rm H_2$ and $\rm NO_2^-$, which is controlled by their mass transport rate. With the calibrated model, the influence of these variables can be evaluated to explain what controls the $\rm NO_2^-$ flux.

3.2. Effect of catalytic hydrogel thickness on flux

Due to the counter-diffusional nature of the CHMR, where the reactants $\rm H_2$ and $\rm NO_2^-$ diffuse from opposite sides into the hydrogel, the hydrogel thickness can have a significant impact on the $\rm NO_2^-$ flux. Fig. 4 shows the $\rm NO_2^-$ flux as a function of hydrogel thickness for various Pd densities. The influent flowrate, influ-

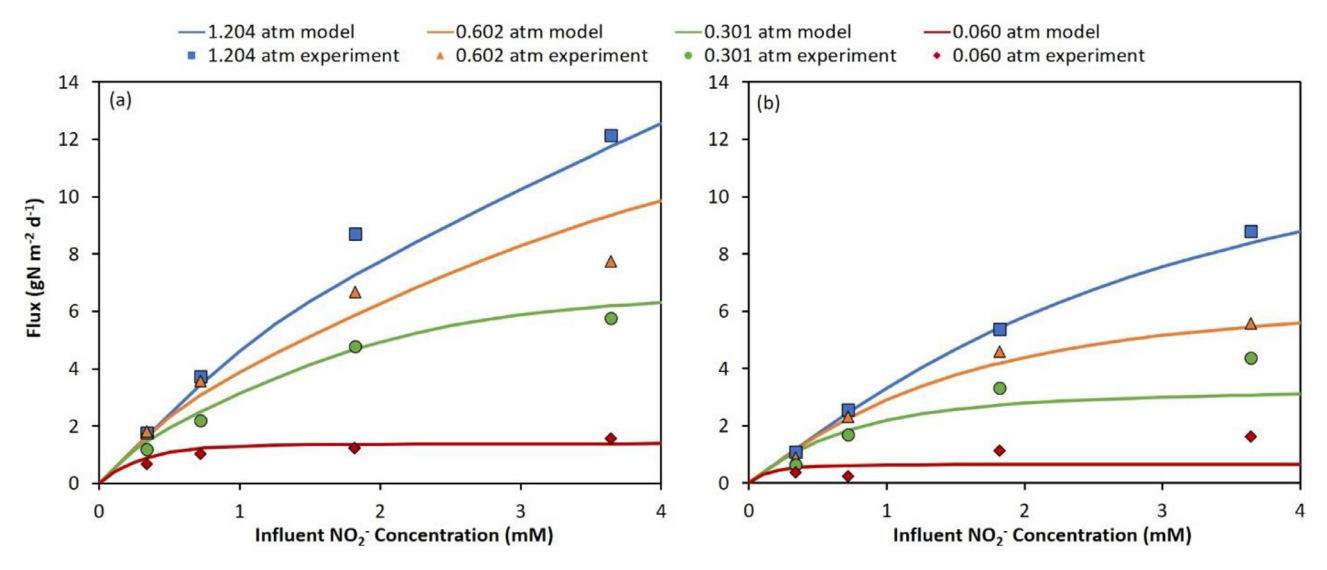


Fig. 3. NO_2^- flux as a function of influent NO_2^- concentration for the computational model (lines) and experimental data (points). (a) 137.2 mole-Pd m⁻³_{hydrogel}. (b) 31.99 mole-Pd m⁻³_{hydrogel}.

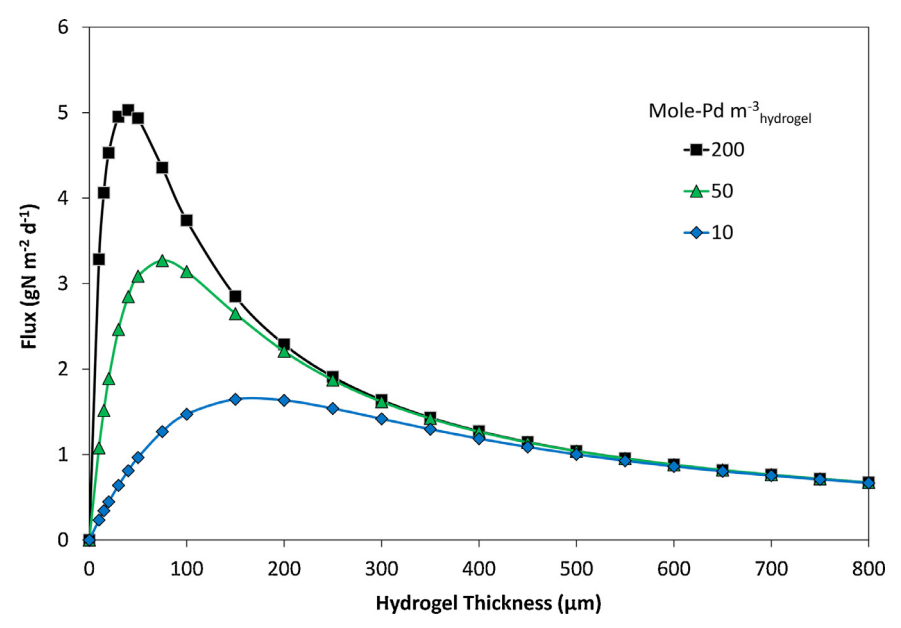


Fig. 4. NO_2^- flux as a function of the hydrogel thickness for three Pd densities.

ent NO_2^- concentration, and H_2 supply pressure are constant. A higher Pd density results in increased flux for all conditions, but for hydrogels above approximately 500 μ m, increasing the Pd density does not provide appreciable increases in flux. This is due to the low availability of H_2 and NO_2^- at Pd sites. This affects the NO_2^- reduction rate, as explained below.

When the hydrogel thickness is large, the concurrent reactant concentrations are low due to mass transport resistance in the hydrogel. Thus, the flux is low. However, decreasing the hydrogel thickness does not guarantee increased flux. If the hydrogel is too thin, the available Pd active sites becomes limiting. For all Pd densities tested, the optimal flux occurs when the hydrogel thickness is between 30 and 150 μm , and the optimal thickness for peak flux decreases with increasing Pd density. As such, some outer catalyst bearing layer is required and simply adding catalyst directly to the surface of the HFM will not provide efficient reaction conditions.

Note, the optimal thickness range will also change if the influent flow, influent NO₂⁻, and supplied H₂ are changed. Given a set of conditions, this model can be used to determine the optimal hy-

drogel thickness that can guide improved synthesis of the CHMR. The impact of hydrogel thickness of the flux can be explained by evaluating the $\rm H_2$ and $\rm NO_2^-$ concentration and $\rm NO_2^-$ reduction rate profiles within the hydrogel.

3.3. Effect of the hydrogel thickness and Pd density on the NO_2^- and H_2 concentrations and NO_2^- reduction rate in the hydrogel profile

As described by Eq. (3), the NO_2^- reduction rate is dependent on the concentrations of NO_2^- , H_2 , and Pd density in the hydrogel. Thus, this reaction only occurs in the catalytic hydrogel in regions where H_2 and NO_2^- are concurrent, defined herein as the reactive zone (RZ). In this region, the flux of H_2 and NO_2^- are influenced by both Fickian diffusion (Eq. (2)) and the NO_2^- reduction rate (Eq. (3)), which are dependent on localized H_2 and NO_2^- concentrations. Transport of H_2 or NO_2^- in the catalytic hydrogel where the opposing reactant is not present is governed solely by diffusion, and this region is termed herein as the non-reactive zone (NRZ).

Due to the counter-diffusional nature of the CHMR, the hydrogel thickness impacts the concurrent H_2 and NO_2^- concentrations

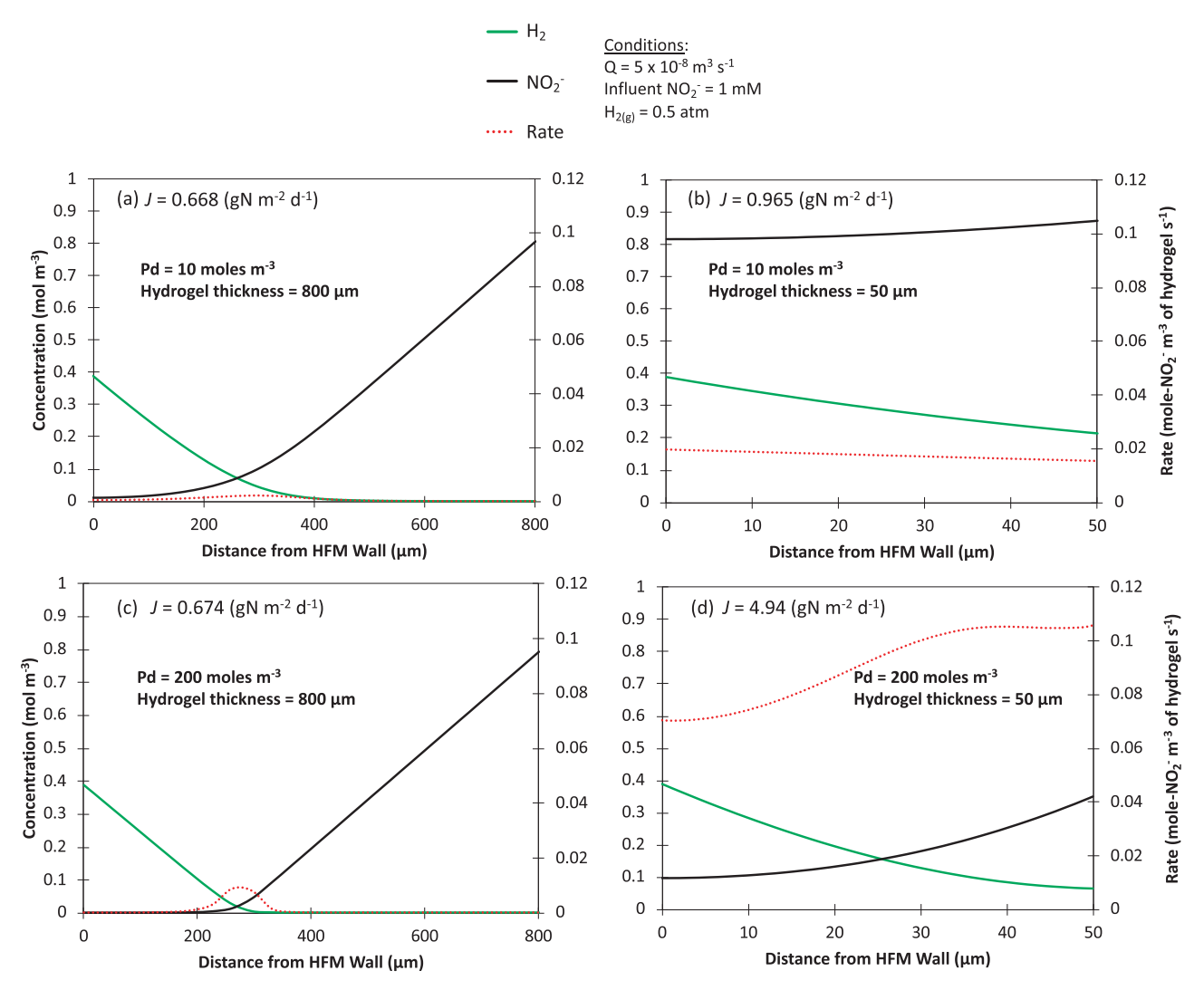


Fig. 5. H_2 and NO_2^- concentration and NO_2^- reduction rate profiles in the hydrogel for hydrogel thicknesses of (a, c) 800 μ m and (b, d) 50 μ m and Pd densities of (a, b) 10 mole-Pd m^{-3} and (c, d) 200 mole-Pd m^{-3} .

in the hydrogel. This in turn affects the localized reaction rate at Pd sites and thus flux. Fig. 5 shows the $\rm H_2$ and $\rm NO_2^-$ concentration and $\rm NO_2^-$ reduction rate profiles for two hydrogel thicknesses (thick = 800 µm and thin = 50 µm) and two Pd densities (200 and 10 mole-Pd $\rm m^{-3}_{hydrogel}$). Using the results from Fig. 4, the two thicknesses were chosen to represent a thinner hydrogel that is affected by the Pd density and a thicker hydrogel that is less sensitive to Pd density. The influent flowrate, influent $\rm NO_2^-$ concentration, and $\rm H_2$ supply pressure are constant and are the same as that in Fig. 4.

For a thick hydrogel (Fig. 5a and c; Fig. SI-2a), the reactant concentration profiles are dominated by mass transport limitations. $\rm H_2$ and $\rm NO_2^-$ must diffuse far into the hydrogel before meeting at Pd active sites. For the low Pd density (Fig. 5a), this results in a broad RZ (~500 μm) with respect to the total thickness (800 μm) and low $\rm H_2$ and $\rm NO_2^-$ concentrations in the RZ, resulting in low $\rm NO_2^-$ reduction rates. For the high Pd density (Fig. 5c), the $\rm NO_2^-$ reduction rates are higher because there are more Pd active sites, but this causes the RZ to become narrower (~200 μm). The flux is the sum of all the rates within the hydrogel, i.e., the integral of the RZ. Thus, only insignificant increases in flux occur when increasing the Pd density due to mass transfer limitations of the thicker hydrogel. For example, the flux for the 200 and 10 mole-Pd $\rm m^{-3}_{hydrogel}$

densities are 0.674 and 0.668 gN m $^{-2}$ d $^{-1}$, or a <1% difference. This confirms the results from Fig. 4 showing a convergence of the fluxes for the Pd densities with increasing thickness. Thus, for thick hydrogels, much of the hydrogel is either NO $_2$ or H $_2$ concentration limited (i.e., the NRZ), and only a small portion of the Pd is being used.

For thin hydrogels (Fig. 5b and d; Fig. SI-2b), $\rm H_2$ and $\rm NO_2^-$ are present throughout the hydrogel layer and the RZ encompasses the full hydrogel profile for all Pd densities tested. Because all the Pd in the hydrogel is being used, increasing the Pd density results in a higher $\rm NO_2^-$ reduction rate throughout the hydrogel layer. Though, for higher densities, the reaction starts to become $\rm NO_2^-$ limited closer to the HFM wall (Fig. 5d; Fig. SI-2). Increasing the Pd density leads to noticeable increases in flux. For example, the flux for the 200 and 10 mole-Pd $\rm m^{-3}_{hydrogel}$ densities is 4.94 and 0.965 gN $\rm m^{-2}$ d⁻¹, respectively.

3.4. Effect of the NO_2^- and H_2 concentrations on the concentration and rate profiles

One of the major benefits of the CHMR over conventional three-phase catalyst systems is the ability to control the $\rm H_2$ supply pressure to maintain an optimal rate and conversion. In realistic oper-

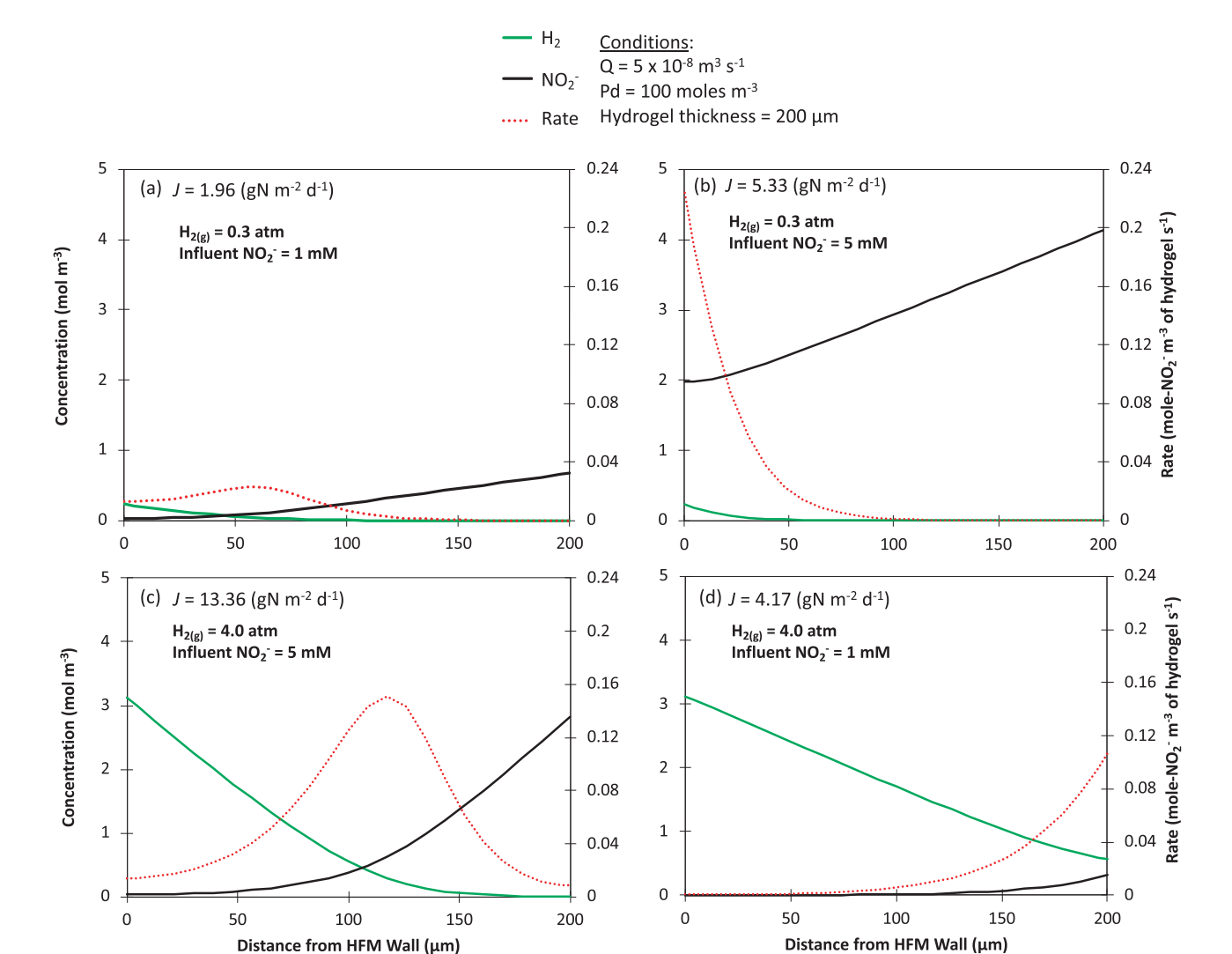


Fig. 6. H₂ and NO₂⁻ concentration and NO₂⁻ rate profiles for different H₂ partial pressures and influent NO₂⁻ concentrations. The Pd density (100 mole $m^{-3}_{hydrogel}$) and hydrogel thickness (200 μm). The left y-axis in all plots corresponds to the H₂ and NO₂⁻ concentrations (mM); solid lines. The right y-axis on all plots corresponds to the NO₂⁻ reduction rate (mole-NO₂⁻ $m^{-3}_{hydrogel}$ s⁻¹); dotted line. The x-axis represents the distance from the HFM wall; the left edge is the HFM wall and the right edge is the LDL/bulk solution.

ating situations the Pd density will be relatively constant, but the influent NO_2^- concentration may have seasonal changes. The H_2 partial pressure can be easily adjusted to match fluctuating NO_2^- concentrations. Further, as seen in Fig. 5, the H_2 and NO_2^- concentrations can greatly impact the overall reaction rate.

Fig. 6 demonstrates four scenarios for combinations of low and high influent $\rm H_2$ and $\rm NO_2^-$ concentrations. The influent flowrate, Pd density, and hydrogel thickness were constant. A hydrogel thickness of 200 μm was chosen so the reactant profiles and changes in the $\rm NO_2^-$ rate can be easily distinguished with reactant concentration changes.

When the influent NO_2^- concentration (1 mM) and H_2 supply pressure (0.3 atm) are relatively low, the peak NO_2^- reduction rate is low and the RZ is narrow (Fig. 6a). This results in a flux of 1.96 gN m⁻² d⁻¹. If the influent NO_2^- concentration increases to 5 mM with no change in the H_2 supply pressure (Fig. 6b), then the H_2 becomes limiting, resulting in an RZ that is shifted toward the HFM. But, because the available NO_2^- is higher, higher NO_2^- reduction rates are achieved across a narrower RZ, resulting in a flux increase to 5.33 gN m⁻² d⁻¹. If the H_2 supply pressure is increased to 4.0 atm to match the increasing influent NO_2^- (5 mM) (Fig. 6c), then the RZ broadens while maintaining a high peak NO_2^- reduc-

tion rate. This results again in a flux increase to 13.36 gN m $^{-2}$ d $^{-1}$. However, a higher H $_2$ supply pressure is not always better. If the H $_2$ remains at 4.0 atm but the influent NO $_2$ $^-$ drops back down to 1 mM (Fig. 6d), then the RZ is shifted toward the bulk. While an increased flux is observed (1.96 to 4.17 gN m $^{-2}$ d $^{-1}$), there is still H $_2$ remaining at the hydrogel-bulk interface. This results in wasted H $_2$, and the excess H $_2$ can diffuse into the bulk, which may promote the growth of bacterial biofilms that use H $_2$ as an electron donor substrate. Thus, as depicted by the modeling results, the ability to control the H $_2$ feed pressure such that H $_2$ remains optimal throughout the RZ is an advantage of the CHMR compared to other catalytic reactors.

4. Conclusions

This study focused on development of a 1-D model to describe the CHMR. This model can be used to evaluate the overall contaminant removal rate (i.e., flux), the H₂ and contaminant concentrations within the hydrogel, and the contaminant removal rates within the hydrogel. This model can be extended to any hydrogenation catalyst (e.g., Rh, Ru, Pd-In) or reactant (e.g., nitrate, bromate, perchlorate, trichloroethylene), allowing for the input of

different reaction expressions and reactor conditions. The model can also be extended to other ICMRs that comprise of a mixed gas compartment linked diffusively to a catalytic layer that is analogous to a biofilm.

To improve the CHMR model for NO₂⁻ (or NO₃⁻) hydrogenation, we suggest incorporating the effects of pH on catalytic activity. Basic pH greatly inhibits the reaction, and because OH- is a reaction byproduct, the reaction is naturally inhibited unless pH control is employed (Ebbesen et al., 2011; Matatov-Meytal et al., 2003). CO₂ bubbling is a simple buffer that can prevent a pH increase and can be included in the model either in the HFM or hydrogel reactor compartment. Inclusion of O₂ in the model is another possible improvement, as O₂ will react with H₂ preferentially over Pd catalysts, forming H2O2 and H2O, which may affect reaction kinetics if there is sufficient competition with NO_2^- for active sites (Centi et al., 2003). Another critical aspect of NO₂-/NO₃- hydrogenation is selectivity. Inclusion of NH₄⁺ formation in a model is likely not viable considering the current limited understanding of the reaction pathway (Hu et al., 2018). Future work developing this understanding for inclusion would greatly enhance the value of such a model, as the ability of the system to maintain NH_{Δ}^{+} concentrations below regulated levels is critical for drinking water applications. Finally, the model could be improved by including a wider range of reactant concentrations, along with further validation of the model through experimental repetitions.

Development of a two-dimensional (2-D) model will greatly enhance the capabilities of a model to properly predict CHMR performance in real-world conditions. It would provide information about changes along the axial and latitudinal positions within the CHMR. This would allow for investigation of the development of H₂ concentration gradients that occur when the HFM lumen is supplied with H₂ in open or closed mode operation (Marks et al., 2020). The benefits of periodic venting of the HFM lumen on H₂ consumption efficiency while maintaining high catalytic activity have been demonstrated experimentally for CHMRs and through modeling of membrane biofilm reactors (Perez-Calleja et al., 2017). Development of a 2-D model in a program such as COMSOL would allow for optimization of the venting procedure to maximize the critical venting parameters of vent period and interval. Additionally, the 2-D model could be used to evaluate contaminant concentration gradients along the axial flow of the CHMR.

Declaration of Competing Interest

The authors declare that they have no known competing financial interests or personal relationships that could have appeared to influence the work reported in this paper.

Acknowledgements

This material is based upon work supported by the National Science Foundation under grant no. CBET-1847466. Additional support for Randal Marks came from the CEST/Bayer Predoctoral Research Fellowship [Center for Environmental Science and Technology at Notre Dame (CEST)] and the Patrick and Jana Eilers Graduate Student Fellowship for Energy Related Research [Center for Sustainable Energy at Notre Dame (ND Energy)].

Supplementary materials

Supplementary material associated with this article can be found, in the online version, at doi:10.1016/j.watres.2020.116199.

References

Aran, H.C., Benito, S.P., Luiten-Olieman, M.W.J., Er, S., Wessling, M., Lefferts, L., Benes, N.E., Lammertink, R.G.H., 2011. Carbon nanofibers in catalytic membrane microreactors. J. Membr. Sci. 381 (1–2), 244–250.

- Benjamin, M.M. (2015) Water Chemistry.
- Bergquist, A.M.B., Madison, Gildert, Gary, Strathmann, Timothy J., Werth, Charles J., 2017. Catalytic denitrification in a trickle bed reactor: ion exchange waste brine treatment. Am. Water Works Assoc. 109 (Number 5), E129–E143.
- Bertoch, M., Bergquist, A.M., Gildert, G., Strathmann, T.J., Werth, C.J., 2017. Catalytic nitrate removal in a trickle bed reactor: direct drinking water treatment. J. Am. Water Works Assoc. 109 (5), E144–E157.
- Brindle, K., Stephenson, T., Semmens, M.J., 1998. Nitrification and oxygen utilisation in a membrane aeration bioreactor. J. Membr. Sci. 144 (1–2), 197–209.
- Buonomenna, M.G., Choi, S.H., Drioli, E., 2010. Catalysis in polymeric membrane reactors: the membrane role. Asia-Pac. J. Chem. Eng. 5 (1), 26–34.
- Centi, G., Dittmeyer, R., Perathoner, S., Reif, M., 2003. Tubular inorganic catalytic membrane reactors: advantages and performance in multiphase hydrogenation reactions. Catal. Today 79 (1–4), 139–149.
- reactions. Catal. Today 79 (1–4), 139–149.
 Chaplin, B.P., Reinhard, M., Schneider, W.F., Schuth, C., Shapley, J.R., Strathmann, T.J.,
 Werth, C.J., 2012. Critical review of Pd-based catalytic treatment of priority contaminants in water. Environ. Sci. Technol. 46 (7), 3655–3670.
- Chen, Y.X., Zhang, Y., Liu, H.Y., 2003. Reduction of nitrate from groundwater: powder catalysts and catalytic membrane. J. Environ. Sci. 15 (5), 600–606.
- Choe, J.K., Bergquist, A.M., Jeong, S., Guest, J.S., Werth, C.J., Strathmann, T.J., 2015. Performance and life cycle environmental benefits of recycling spent ion exchange brines by catalytic treatment of nitrate. Water Res. 80, 267–280.
- Chung, J., Nerenberg, R., Rittmann, B.E., 2006. Bioreduction of selenate using a hydrogen-based membrane biofilm reactor. Environ. Sci. Technol. 40 (5), 1664–1671.
- Daub, K., Emig, G., Chollier, M.J., Callant, M., Dittmeyer, R., 1999. Studies on the use of catalytic membranes for reduction of nitrate in drinking water. Chem. Eng. Sci. 54 (10), 1577–1582.
- Dittmeyer, R., Hollein, V., Daub, K., 2001. Membrane reactors for hydrogenation and dehydrogenation processes based on supported palladium. J. Mol. Catal. a-Chem. 173 (1–2), 135–184.
- Dittmeyer, R., Svajda, K., Reif, M., 2004. A review of catalytic membrane layers for gas/liquid reactions. Top. Catal. 29 (1–2), 3–27.
- Ebbesen, S.D., Mojet, B.L., Lefferts, L., 2011. Effect of pH on the nitrite hydrogenation mechanism over Pd/Al₂O₃ and Pt/Al₂O₃: details obtained with ATR-IR spectroscopy. J. Phys. Chem. C 115 (4), 1186–1194.
- Espinosa, R.B., Rafieian, D., Lammertink, R.G.H., Lefferts, L., 2016. Carbon nano-fiber based membrane reactor for selective nitrite hydrogenation. Catal. Today 273, 50–61.
- Espinosa, R.B., Rafieian, D., Postma, R.S., Lammertink, R.G.H., Lefferts, L., 2018. Egg-shell membrane reactors for nitrite hydrogenation: manipulating kinetics and selectivity. Appl. Catal. B-Environ. 224, 276–282.
- Essila, N.J., Semmens, M.J., Voller, V.R., 2000. Modeling biofilms on gas-permeable supports: concentration and activity profiles. J. Environ. Eng.-Asce 126 (3), 250–257.
- Ferrell, R.T., Himmelblau, D.M., 1967. Diffusion coefficients of hydrogen and helium in water. AIChE J. 13 (4) 702-&.
- Guo, S.J., Heck, K., Kasiraju, S., Qian, H.F., Zhao, Z., Grabow, L.C., Miller, J.T., Wong, M.S., 2018. Insights into nitrate reduction over indium-decorated palladium nanoparticle catalysts. Acs Catal. 8 (1), 503–515.
- Hibiya, K., Terada, A., Tsuneda, S., Hirata, A., 2003. Simultaneous nitrification and denitrification by controlling vertical and horizontal microenvironment in a membrane-aerated biofilm reactor. J. Biotechnol. 100 (1), 23–32.
- Hinshelwood, C.N.S., 1940. The Kinetics of Chemical Change. The Clarendon press, Oxford.
- Hu, M.C., Liu, Y., Yao, Z.H., Ma, L.P., Wang, X.Q., 2018. Catalytic reduction for water treatment. Front. Environ. Sci. Eng. 12 (1).
- Marks, R., Seaman, J., Kim, J., Doudrick, K., 2020. Activity and stability of the catalytic hydrogel membrane reactor for treating oxidized contaminants. Water Res. Under Revision.
- Marks, R., Seaman, J., Perez-Calleja, P., Kim, J., Nerenberg, R., Doudrick, K., 2019. Catalytic hydrogel membrane reactor for treatment of aqueous contaminants. Environ. Sci. Technol. 53 (11), 6492–6500.
- Martin, K.J., Nerenberg, R., 2012. The membrane biofilm reactor (MBfR) for water and wastewater treatment: principles, applications, and recent developments. Bioresour. Technol. 122, 83–94.
- Martin, K.J., Picioreanu, C., Nerenberg, R., 2015. Assessing microbial competition in a hydrogen-based membrane biofilm reactor (MBfR) using multidimensional modeling. Biotechnol. Bioeng. 112 (9), 1843–1853.
- Matatov-Meytal, Y., Shindler, Y., Sheintuch, M., 2003. Cloth catalysts in water denitrification III. pH inhibition of nitrite hydrogenation over Pd/ACC. Appl. Catal. B-Environ. 45 (2), 127–134.
- Merkel, T.C., Bondar, V.I., Nagai, K., Freeman, B.D., Pinnau, I., 2000. Gas sorption, diffusion, and permeation in poly(dimethylsiloxane). J. Polym. Sci. Part B-Polym. Phys. 38 (3), 415–434.
- Nerenberg, R., 2016. The membrane-biofilm reactor (MBfR) as a counter-diffusional biofilm process. Curr. Opin. Biotechnol. 38, 131–136.
- Nerenberg, R., Rittmann, B.E., 2004. Hydrogen-based, hollow-fiber membrane biofilm reactor for reduction of perchlorate and other oxidized contaminants. Water Sci. Technol. 49 (11–12), 223–230.
- Nerenberg, R., Rittmann, B.E., Najm, I., 2002. Perchlorate reduction in a hydrogen-based membrane-biofilm reactor. J. Am. Water Works Assoc. 94 (11), 103–114.
- Pankhania, M., Brindle, K., Stephenson, T., 1999. Membrane aeration bioreactors for wastewater treatment: completely mixed and plug-flow operation. Chem. Eng. J. 73 (2), 131–136.

- Perez-Calleja, P., Aybar, M., Picioreanu, C., Esteban-Garcia, A.L., Martin, K.J., Nerenberg, R., 2017. Periodic venting of MABR lumen allows high removal rates and high gas-transfer efficiencies. Water Res. 121, 349–360.
- Pintar, A., Bercic, G., Levec, J., 1998. Catalytic liquid-phase nitrite reduction: kinetics and catalyst deactivation. AIChE J. 44 (10), 2280–2292.
- Postma, R.S., Espinosa, R.B., Lefferts, L., 2018. Competitive adsorption of nitrite and hydrogen on palladium during nitrite hydrogenation. ChemCatChem 10 (17), 3770-3776.
- Reichert, P., 1994. Aquasim a tool for simulation and data-analysis of aquatic systems. Water Sci. Technol. 30 (2), 21–30. Sabba, F., Picioreanu, C., Nerenberg, R., 2017. Mechanisms of nitrous oxide (N₂O)
- formation and reduction in denitrifying biofilms. Biotechnol. Bioeng. 114 (12), 2753-2761
- Semmens, M.J., Essila, N.J., 2001. Modeling biofilms on gas-permeable supports: flux limitations. J. Environ. Eng.-Asce 127 (2), 126-133.

- Shelstad, K.A., Downie, J., Graydon, W.F., 1960. Kinetics of the vapor-phase oxidation of napthalene over a vanadium catalyst. Can. J. Chem. Eng. (August) 102-107.
- Stewart, P.S., 2003. Diffusion in biofilms. J. Bacteriol. 185 (5), 1485-1491.
- Strukul, G., Gavagnin, R., Pinna, F., Modaferri, E., Perathoner, S., Centi, G., Marella, M., Tomaselli, M., 2000. Use of palladium based catalysts in the hydrogenation of nitrates in drinking water: from powders to membranes. Catal. Today 55 (1-2), 139-149.
- Syron, E., Casey, E., 2008. Membrane-aerated biofilms for high rate biotreatment: performance appraisal, engineering principles, scale-up, and development requirements. Environ. Sci. Technol. 42 (6), 1833–1844.
- Wanner, O., Morgenroth, E., 2004. Biofilm modeling with AQUASIM. Water Sci. Technol. 49 (11-12), 137-144.
- Ziv-El, M.C., Rittmann, B.E., 2009. Systematic evaluation of nitrate and perchlorate bioreduction kinetics in groundwater using a hydrogen-based membrane biofilm reactor. Water Res. 43 (1), 173–181.